Star Formation in the Dwarf Seyfert Galaxy NGC 4395: Evidence for Both AGN and SN Feedback?

Payel Nandi[1,2], C. S. Stalin[1] , D. J. Saikia[3] , S. Muneer[1] , George Mountrichas[4], Dominika Wylezalek[5] , R. Sagar[1] , and Markus Kissler-Patig[6]

[1] Indian Institute of Astrophysics, Block II, Koramangala, Bangalore, India; payel.nandi@iiap.res.in
[2] Indian Institute of Science, Bangalore, India
[3] Inter-University Centre for Astronomy and Astrophysics (IUCAA), Post Bag 4, Ganeshkhind, Pune 411 007, India
[4] Instituto de Fisica de Cantabria (CSIC-Universidad de Cantabria), Avenida de los Castros, E-39005 Santander, Spain
[5] Astronomisches Rechen-Institu, Univeristy of Heidelberg, D-69120 Heidelberg, Germany
[6] European Space Agency (ESA), European Space Astronomy Centre (ESAC), Camino Bajo del Castillo s/n, E-28692 Villanueva de la Cañada, Madrid, Spain

Abstract

We present a detailed multiwavelength study of star formation in the dwarf galaxy NGC 4395, which hosts an active galactic nucleus (AGN). From our observations with the Ultra-Violet Imaging Telescope, we have compiled a catalog of 284 star-forming (SF) regions, out of which we could detect 120 SF regions in Hα observations. Across the entire galaxy, we found the extinction-corrected star formation rate (SFR) in the far ultraviolet (UV) to range from $2.0 \times 10^{-5} \, M_\odot \, \mathrm{yr}^{-1}$ to $1.5 \times 10^{-2} \, M_\odot \, \mathrm{yr}^{-1}$ with a median of $3.0 \times 10^{-4} \, M_\odot \, \mathrm{yr}^{-1}$, and the age to lie in the range of ∼1 to 98 Myr with a median of 14 Myr. In Hα we found the SFR to range from $7.2 \times 10^{-6} \, M_\odot \, \mathrm{yr}^{-1}$ to $2.7 \times 10^{-2} \, M_\odot \, \mathrm{yr}^{-1}$ with a median of $1.7 \times 10^{-4} \, M_\odot \, \mathrm{yr}^{-1}$, and the age to lie between 3 to 6 Myr with a median of 5 Myr. The stellar ages derived from Hα show a gradual decline with galactocentric distance. We found three SF regions close to the center of NGC 4395 with high SFRs both from Hα and UV, which could be attributed to feedback effects from the AGN. We also found six other SF regions in one of the spiral arms having higher SFRs. These are very close to supernova remnants, which could have enhanced the SFR locally. We obtained a specific SFR (SFR per unit mass) for the whole galaxy of $4.64 \times 10^{-10} \, \mathrm{yr}^{-1}$.

1. Introduction

In the Seyfert category of active galactic nuclei (AGNs), circumnuclear star formation is commonly observed (Davies et al. 1998; Álvarez-Álvarez et al. 2015; Hennig et al. 2018; Diniz et al. 2019). However, works to clarify the relationships between the central AGN and star formation in their surroundings are still ongoing. There are suggestions for causal and evolutionary connections. The difficulty in establishing the connection is due to differences in the spatial and temporal scales between AGN and starburst activities. Available studies on AGN hosts probe star formation on scales of kiloparsecs to a few hundreds of parsecs (Venturi et al. 2021; Riffel et al. 2022). However, accretion processes that feed the AGN occur on scales of the order of parsecs. The influence AGNs have on their host galaxies is expected to decrease with an increase in the distance of the regions from the central AGN (Tsai & Hwang 2015). Therefore, to establish a connection between AGN and star formation activities, one needs to probe different spatial scales in the hosts of AGNs.

The star formation rate (SFR) of a galaxy is an important parameter. Several SFR measures are available in the literature (Kennicutt & Evans 2012; Calzetti 2013). Observationally, the star formation nature of a galaxy can be characterized by measuring its luminosity, which can then be used to find the number of O and B stars. Because of their high luminosity and temperature, ultraviolet (UV) observations are the most straightforward SFR indicator. Alternatively, Hα observations in the optical are generally used to estimate the SFR (Kennicutt 1998). As UV photons, and to a lesser extent optical photons, are affected by dust attenuation, observations at other wavelengths are also used to estimate the SFR. Other estimators of the SFR are via the radio and infrared (IR) emission emitted from star-forming (SF) regions (Kennicutt & Evans 2012; Calzetti 2013). The radio emission from such regions can be due to thermal free–free (bremsstrahlung) and nonthermal (synchrotron) processes (Condon 1992). An advantage of using radio emission to trace the SFR is that it is free from dust extinction, unlike that of observations in the UV and optical bands that are sensitive to dust. There are a number of studies in the literature that focus on the star formation properties of Seyfert type AGNs using optical observations (e.g., Davies et al. 1998; Gu et al. 2001; Hennig et al. 2018). Though observations in the UV band are an alternative tracer to investigate the star formation characteristics of the host galaxies of AGNs, such observations are limited (Colina et al. 1997; Fanelli et al. 1997; Muñoz Marín et al. 2009).

Although the star formation characteristics of galaxies hosting an AGN have been studied reasonably extensively, similar studies for dwarf galaxies with $M_* < 10^{10} \, M_\odot$ are extremely limited. Understanding the nature of star formation in AGN-hosting dwarf galaxies is important as these systems are expected to be powered by small- or intermediate-mass

black holes (Reines 2022). Studies of such objects in the nearby universe may provide valuable insights in understanding how similar objects may have evolved in the early universe. Earlier, theoretical studies on the regulation of star formation in dwarf galaxies have been attributed to radiation from young stars and supernova (SN) explosions (Benson et al. 2002). However, recent theoretical studies do indicate that AGNs could play a significant role in regulating star formation in dwarf galaxies (Koudmani et al. 2022). Observationally, there is evidence of AGN feedback operating in dwarf galaxies covering angular sizes smaller than about an arcminute (Penny et al. 2018). In addition to such studies, it is also important to extend similar studies to a large range of spatial scales. Also, close correlations are known to exist between the masses of supermassive black holes that power AGNs and various properties of their host galaxies (Kormendy & Richstone 1995; Magorrian et al. 1998; Ferrarese & Merritt 2000; Gebhardt et al. 2000; Gültekin et al. 2009). Dwarf galaxies with smaller black hole masses appear to follow the same scaling relationships as of higher mass galaxies, although with a larger scatter. These correlations and studies of the effects of jets also suggest that AGNs can influence their galaxies through feedback processes (Fabian 2012; Venturi et al. 2021). Though AGN feedback effects are observationally known in massive galaxies such as AGNs inhibiting as well as enhancing star formation, observational evidences for AGN feedback in dwarf galaxies is very limited (Penny et al. 2018; Baldassare et al. 2020; Greene et al. 2020; Schutte & Reines 2022). Therefore, detailed studies on the star formation characteristics of dwarf galaxies hosting AGNs are needed, first, to characterize their star formation properties and second to find evidence of the feedback processes, if any, in them.

NGC 4395 is a nearby dwarf galaxy situated at a distance of 4.3 Mpc (Thim et al. 2004). It hosts a low-luminosity Seyfert type AGN and is powered by a black hole with a mass between 10^4 and 10^5 $M_\odot$. For example, from reverberation mapping observations in the UV band carried out with the Space Telescope Imaging Spectrograph on the Hubble Space Telescope, Peterson et al. (2005) found the mass of the black hole in NGC 4395 to be $M_{BH} = (3.6 \pm 1.1) \times 10^5$ $M_\odot$. However, recently, using the response of the Hα emission line to the variations in the V-band continuum, Woo et al. (2019) found a lower value of $M_{BH} = (9.1^{+1.5}_{-1.6} \times 10^3)$ $M_\odot$. NGC 4395 shows other characteristics of Seyfert 1 galaxies, such as variable emission in the optical and X-rays (Lira et al. 1999) and a collimated radio structure with components on opposite sides of the galaxy nucleus (Wrobel et al. 2001; Saikia et al. 2018; Yang et al. 2022). However, it has been found to have a low bolometric luminosity between 10^{40} and 10^{41} erg s^{-1} (Lira et al. 1999; Filippenko & Ho 2003; Brum et al. 2019).

Smirnova et al. (2020) have identified about a hundred SF regions in NGC 4395 from Hα observations with an angular resolution of 2″9, and have made a limited study of comparing their IR fluxes and UV surface brightnesses using archival Galaxy Evolution Explorer (GALEX) data. However, for a detailed understanding of the star formation in this galaxy, deeper and higher resolution observations in the UV and a multiwavelength approach, including radio, are required. We, therefore, carried out a detailed investigation of the star formation in NGC 4395 using our UV observations on scales of a few hundreds of parsecs to a few kiloparsecs. In addition to UV, we also observed NGC 4395 in Hα, and analyzed the nature of those SF regions identified in

Table 1
Details of the Galaxy NGC 4395

Parameter	Value	Reference
R.A.(J2000)	12:25:48.860	Gaia Collaboration et al. (2022)
Decl.(J2000)	+33:32:48.711	Gaia Collaboration et al. (2022)
z	0.00106	Haynes et al. (1998)
Morphology	SA(s)m	de Vaucouleurs et al. (1991)
Semimajor axis	6′.59	de Vaucouleurs et al. (1991)
Semiminor axis	5′.48	de Vaucouleurs et al. (1991)
Position angle	147°	de Vaucouleurs et al. (1991)
Type	Seyfert 1	Filippenko & Sargent (1989)
Stellar mass	2.5×10^9 $M_\odot$	Smirnova et al. (2020)
Distance	4.3 Mpc	Thim et al. (2004)
Inclination angle	38°	Filippenko & Sargent (1989)

the UV using multiwavelength data. In Section 2, we describe the observations and the data reduction procedures. Section 3 describes the identification of the SF regions. The properties of the detected SF regions, along with the global star formation properties of the galaxy are presented in Section 4. A discussion of the results are presented in Section 5, which is followed by a summary in the final section. In this work, we consider a flat ΛCDM cosmology with $H_0 = 70$ km^{-1} s^{-1} Mpc^{-1}, $\Omega_\Lambda = 0.7$, and $\Omega_m = 0.3$.

2. Observations and Data Reduction

For this work, we used our new observations (UV and Hα) as well as archival data (radio, IR, and broadband optical).

2.1. UV

We observed NGC 4395 in the UV band using the Ultra-Violet Imaging Telescope (UVIT; Tandon et al. 2017), one of the payloads on board AstroSat India's first multiwavelength astronomical observatory (Agrawal 2006) launched by the Indian Space Research Organization (ISRO) in 2015 September. The details of the source are given in Table 1. UVIT observes simultaneously in three channels, namely far-UV (FUV; 1300–1800 Å), near-UV, (NUV; 2000–3000 Å), and the visible (VIS; 3200–5500 Å) over a field of view of 28′ diameter with spatial resolution better than 1″5 in the UV. Details of UVIT can be found in Tandon et al. (2020).

NGC 4395 was observed by UVIT on 2018 February 27 in the photon counting mode with the default frame rate of ~34 frames per second. We directly downloaded the level 2 (L2) science-ready images processed using the official L2 pipeline (Ghosh et al. 2022) of the UVIT-Payload Operations Centre at the Indian Institute of Astrophysics, Bangalore and transferred to the Indian Space Science Data Center (ISSDC) for archival and dissemination. In the combined images from ISSDC, we found the exposure time to be lesser than the sum of the individual exposures (orbit-wise images). We therefore based our analysis from the reduced individual L2 images. We first aligned the individual images using the Image Reduction and Analysis Facility (IRAF; Tody 1986) and combined those aligned individual images to create combined, filter-wise images. Astrometry on the combined images was carried out using stars available on the image frames with their (α, δ) positions taken from Gaia-DR3 (Gaia Collaboration et al. 2022) through custom-developed Python scripts. These astrometrically corrected combined image frames were used for further analyses.

Table 2
Log of Observations

Filter Name	Central Wavelength (Å)	Bandwidth (Å)	Telescope	Date of Observation	Exposure Time (s)
F148W	1481	50.0	UVIT	27/02/2018	1348
F172M	1717	12.5	UVIT	27/02/2018	6348
N219M	2196	27.0	UVIT	27/02/2018	6386
N263M	2632	27.5	UVIT	27/02/2018	1355
656.3(10)	6563	10	HCT	22/12/2021	1800
R	6020	1000	HCT	22/12/2021	300

2.2. Optical

Optical observations in the narrow Hα and broad R band were obtained on 2021 December 22, using the Himalayan Faint Object Spectrograph Camera (HFOSC) instrument mounted on the 2 m Himalayan Chandra Telescope (HCT) situated in the Indian Astronomical Observatory, Hanle, India (Prabhu 2014). HFOSC is equipped with a CCD with dimensions of 2048×4096 pixels. The detector has two amplifiers, A and B, which can be operated in both high- and low-gain modes. The readout noise for amplifier A in the high- and low-gain modes are 4.8 electrons and 8.0 electrons, respectively, with gain values of 1.22 electrons ADU^{-1} and 5.6 electrons ADU^{-1}, respectively. The readout noise and gain for amplifier B in the high- and low-gain modes are 5.1 electrons and 8.0 electrons, and 1.21 electrons ADU^{-1} and 5.6 electrons ADU^{-1}, respectively. For imaging, we used amplifier A in the high-gain mode of 1.22 electrons ADU^{-1}. We used only the central 2048×2048 pixels covering a field of view of 10×10 square arcminutes with an image scale of $0\rlap{.}{''}296$ pixel^{-1}. Three exposures each of 600 s or a total of 1800 s was taken in narrowband Hα and one frame of 300 s in the R band. These observations have a spatial resolution between $1\rlap{.}{''}9$ and $2\rlap{.}{''}2$. A log of observations is given in Table 2. Standard procedures were followed to reduce the acquired data, which include bias subtraction, flat-fielding, and cosmic-ray removal using IRAF software (Tody 1986). The three frames in Hα were then combined and astrometrically calibrated using the Gaia-DR3 (Gaia Collaboration et al. 2022) catalog.

For flux calibration in the narrowband Hα we also observed one standard spectrophotometric star, Feige 66. We convolved the observed spectrum of Feige 66 from Oke (1990) with the Hα filter response and estimated the magnitude. The derived magnitude in the Hα observation was converted to a standard magnitude using the difference between the instrumental and standard magnitude of Feige 66. To get the standard magnitude in the R band, we used the technique of differential photometry in conjunction with the relations from the Sloan Digital Sky Survey (SDSS).[7] The transformation equations from SDSS were used to get the standard R-band magnitude of a few stars in the acquired R-band image based on their SDSS u, g, r, i, and z magnitudes. We then subtracted the calibrated R-band image from the calibrated Hα narrowband image to get the calibrated Hα line image as (Waller 1990)

$$f(\text{line}) = \frac{[f_\lambda(N) - f_\lambda(B)]\,W(N)}{[1 - W(N)/W(B)]}. \quad (1)$$

Here, $f_\lambda(N)$ and $f_\lambda(B)$ are the flux densities in the narrow Hα and broad R band, respectively, while $W(N)$ and $W(B)$ are the widths of the narrow Hα and broad R-band filters, respectively. A composite image of NGC 4395 from the R, NUV, and FUV filters covering the central 10×10 square arcminute region is shown in Figure 1.

In addition to the observations acquired in Hα, we also used archival data in the broadband U, B, V, R, and I filters from the Nordic Optical Telescope (NOT). We carried out astrometry as well as photometric calibration on these archival images using the technique of differential photometry.

2.3. IR

In the IR, we used archival images (from NE) in the J, H, and K_s bands from the Two Micron All Sky Survey (2MASS; Skrutskie et al. 2006), and the W1 (3.4 μm), W2 (4.6 μm), and W3 (12 μm) bands taken from the Wide-field Infrared Survey Explorer (WISE; Wright et al. 2010). Also, in the far-IR, we used data at 24, 70, and 160 μm from the Multiband Imaging Photometer for Spitzer (MIPS) instrument (Rieke et al. 2004) on Spitzer. The measurements obtained at these wavelengths were converted to flux units using known scaling factors. For example, in the case of the images from 2MASS, to convert from instrumental measurements to flux units we used the factors given in the respective image headers. For WISE we used the factors available online.[8] Similarly for MIPS, we followed the procedure given in the MIPS instrument handbook.[9]

2.4. Radio

We used observations from the Very Large Array (VLA) carried out at 1.4 GHz in its C configuration. We also have archival data at 1.4 GHz from the VLA in the A and B configurations. However, in the A and B configuration data, only the central AGN is detected. Therefore, in this work we used only the data in the C configuration, the processed image of which was taken from the archives of the VLA.[10] We also used 21 cm H I emission line data from the Westerbork Synthesis Radio Telescope (WSRT; Heald & Oosterloo 2008).

3. Analysis

UVIT observations were carried out in four filters (see Table 2). For analysis, we explicitly used data from all the filters. To calculate the SFR and age we used the F148W and

---

[7] http://sdss.org

[8] https://wise2.ipac.caltech.edu/docs/release/allsky/expsup/sec2_3f.html
[9] https://irsa.ipac.caltech.edu/data/SPITZER/docs/mips/mipsinstrumenthandbook/41/
[10] www.vla.nrao.edu/astro/nvas/
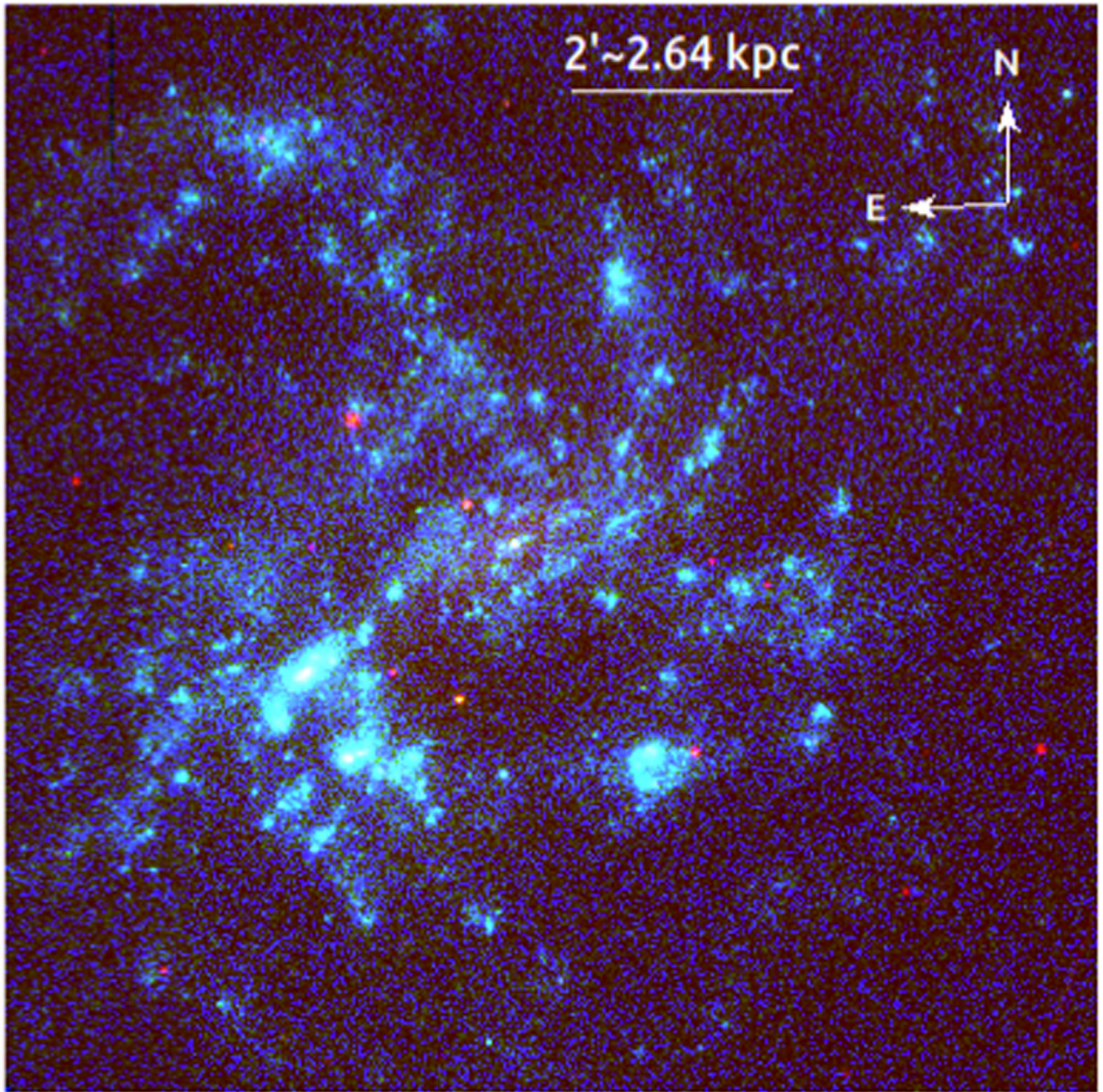
Figure 1. A color composite image of NGC 4395 covering a region of 10×10 square arcminutes. Here, red is the *R*-band image from HCT, green is the NUV image in the N263M filter, and blue is the FUV image in F148W filter. The filter details are in Table 2.

N263M filters as these have a relatively larger effective area (indicative of the overall sensitivity of the photometric system) compared with the other filters. However, for the calculation of color excess, $E(B - V)$ we used one FUV filter (F172M) and one NUV filter (N219M) that are closely spaced in wavelength.

3.1. Identification of SF Regions

To identify SF regions in NGC 4395, we used the final combined image taken in F148W. We used the Source Extractor Software (SExtractor; Bertin & Arnouts 1996) with the following parameters, namely DETECT_THRESH = 5σ, DETECT_MINAREA = 11, and DEBLEND_THRESHOLD = 32. Using the above criteria, we identified a total of 284 SF regions after removal of some overlapping regions. The

identified SF regions marked on the F148W filter image are shown in Figure 2. The same criteria were also used to identify SF regions in the narrowband Hα filter. Out of the 284 regions detected in FUV, we could detect 120 regions that have a sufficient signal-to-noise ratio in the Hα continuum-subtracted image.

3.2. Sizes of the SF Regions

After detecting SF regions, we checked their sizes. SExtractor gives us the semimajor and semiminor lengths in pixel coordinates and position angle in degrees corresponding to each SF region. We converted these to arcseconds and then to parsec units. At the redshift $z = 0.00106$ of NGC 4395, one arcsecond corresponds to 22 pc. The measured sizes of the SF regions in UV and Hα were corrected for their respective
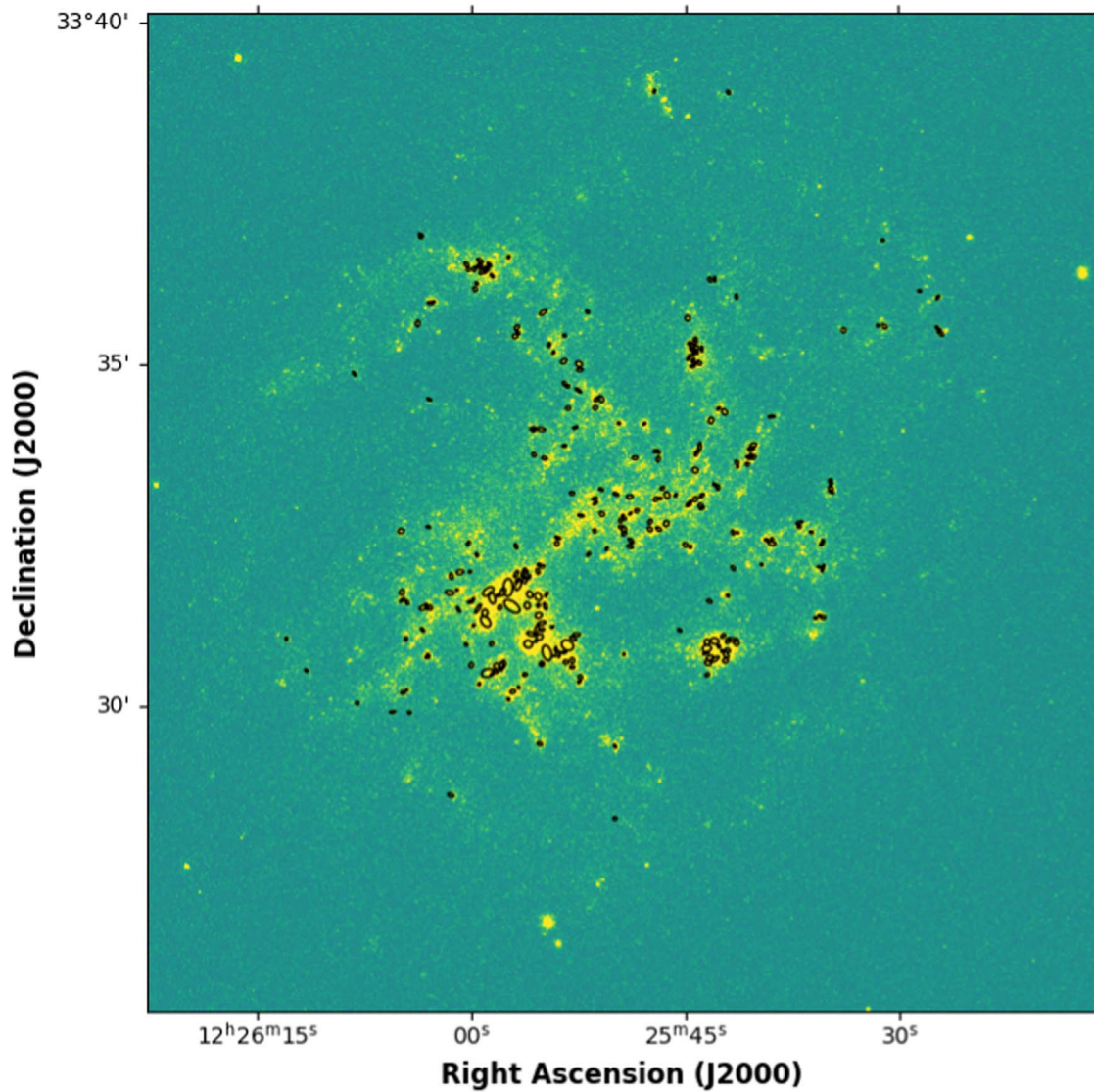
Figure 2. The image of NGC 4395 in the F148W UV filter. The regions that have been identified are marked.

instrumental resolutions by assuming an elliptical light distribution within the apertures. We could correct for instrumental resolution for 225 regions out of 284 detected regions in UV and 77 regions out of 120 regions in Hα. For the remaining regions with sizes similar to the instrumental resolution, we considered the apertures given by SExtractor. We noticed that the areas of the SF regions detected in UV vary from 8.6×10^{-4} kpc^2 to 488.1×10^{-4} kpc^2 with a median of 40.2×10^{-4} kpc^2. The distribution of the areas of the SF regions is shown in Figure 3.

3.3. Photometry

Once the SF regions were identified and the sizes were corrected for instrumental resolution in F148W and Hα using the criteria given in Sections 3.1 and 3.2, we carried out photometry of the regions using the aperture photometry technique in *PhotUtils* (Bradley et al. 2020). As the images in F148W, F172M, N219M, and N263M were astrometrically aligned, photometry of all 284 regions was also carried out on the images
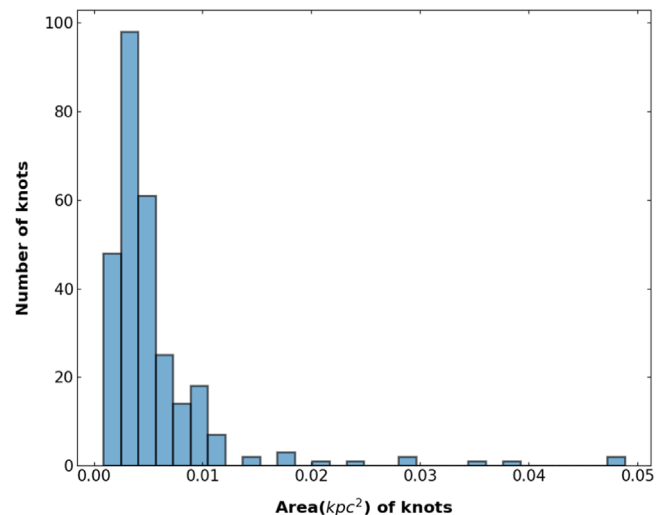
Figure 3. Distribution of the areas of the SF regions identified in FUV.
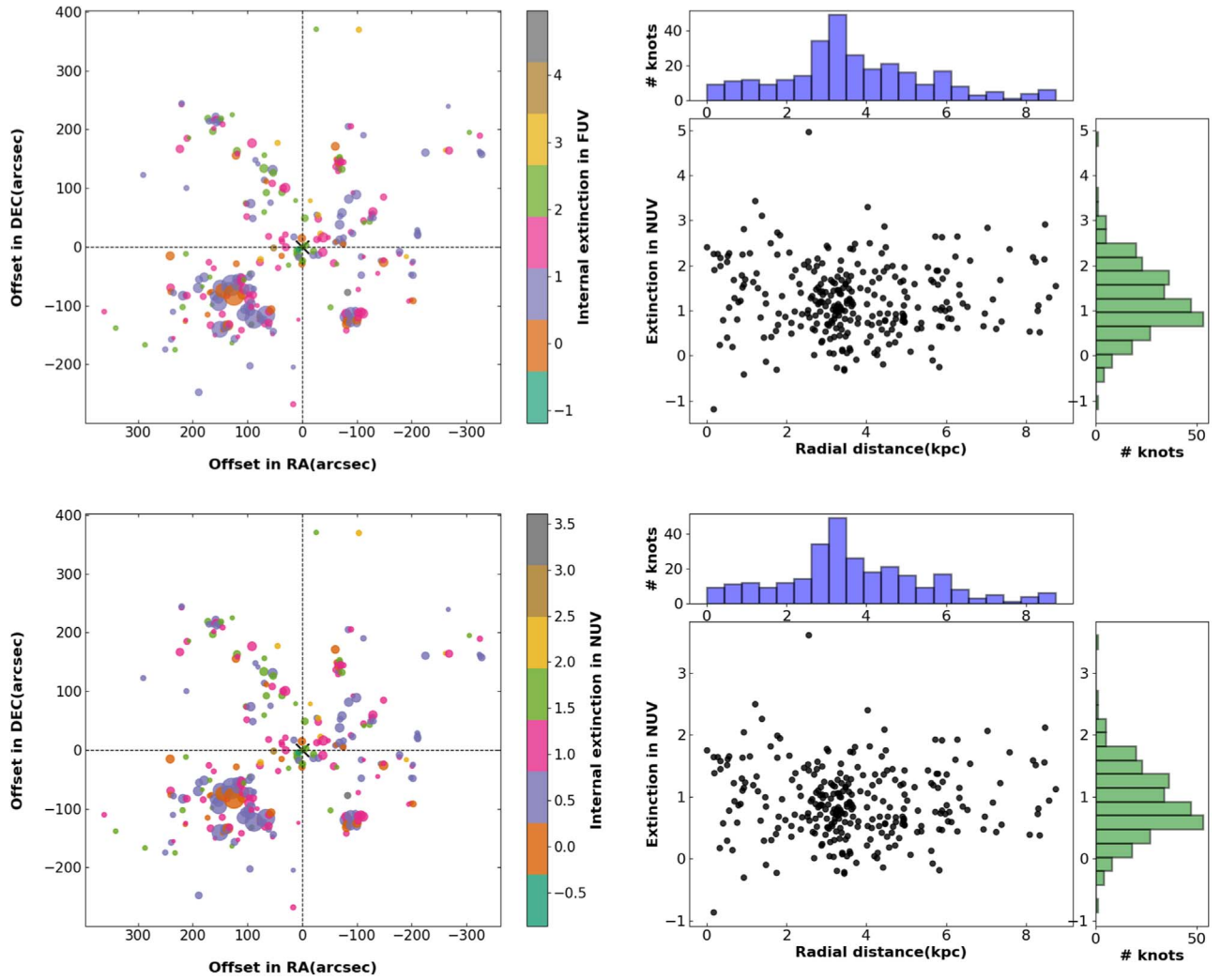
Figure 4. The distribution of internal extinction as well as its spatial variation in the F148W (top panel) and N263M (bottom panel) filters. In the left panels, the different sizes of the points correspond to the sizes of the SF regions.

acquired in all four filters. Similarly, photometry was also carried out in the 120 regions identified in the continuum-subtracted Hα image. One of the crucial parameters for photometry is the proper subtraction of the background. For the determination of the background, we estimated the median count rate in randomly placed square boxes of sizes 10×10 pixels in 50 source-free regions. The mean of these 50 median values was taken as the background per pixel. This background per pixel was subtracted from each of the pixels in the aperture used for photometry. The background-subtracted count rates from each of the identified SF regions in F148W, F172M, N219M, and N263M were converted to magnitudes using the calibration given in Tandon et al. (2020). Similarly, for the Hα observations the derived instrumental magnitudes of the SF regions were converted to standard magnitudes using the procedure outlined in Section 2.2. We note that though the apertures used for the photometry of the SF regions do not overlap, there could be contamination from adjacent SF regions.

3.4. Extinction Correction

The magnitudes derived for the SF regions are affected by both internal and Galactic extinction. To estimate the extinction in UV and Hα for our galaxy, we used the relation given below

(Cardelli et al. 1989)

$$\langle A(\lambda)/A(V) \rangle = a(x) + b(x)/R_v. \qquad (2)$$

Here, $A(V) = 0.047$ mag, is the Galactic extinction in the V band taken from NED,[11] and x is the wavenumber. The values of $a(x)$ and $b(x)$ were evaluated following Cardelli et al. (1989). A similar procedure was also followed to correct for Galactic extinction in the Hα image.

Dust present within each of the detected SF regions scatters and/or absorbs the UV photons coming from those regions, making it difficult to estimate the absolute flux emitted from those regions. To correct for this in the UV band, we used a method based on the UV spectral slope β defined as the slope of the power-law function ($f_\lambda \propto \lambda^\beta$) followed by the continuum emission of galaxies over the wavelength range of $1300-2600$ Å (Calzetti et al. 1994). As this slope can serve as a good diagnostic for internal dust extinction, we adopted this to calculate the internal dust extinction in each of the SF regions. For the FUV and NUV wavelengths used in this work, we calculated β using the

---

[11] http://ned.ipac.caltech.edu
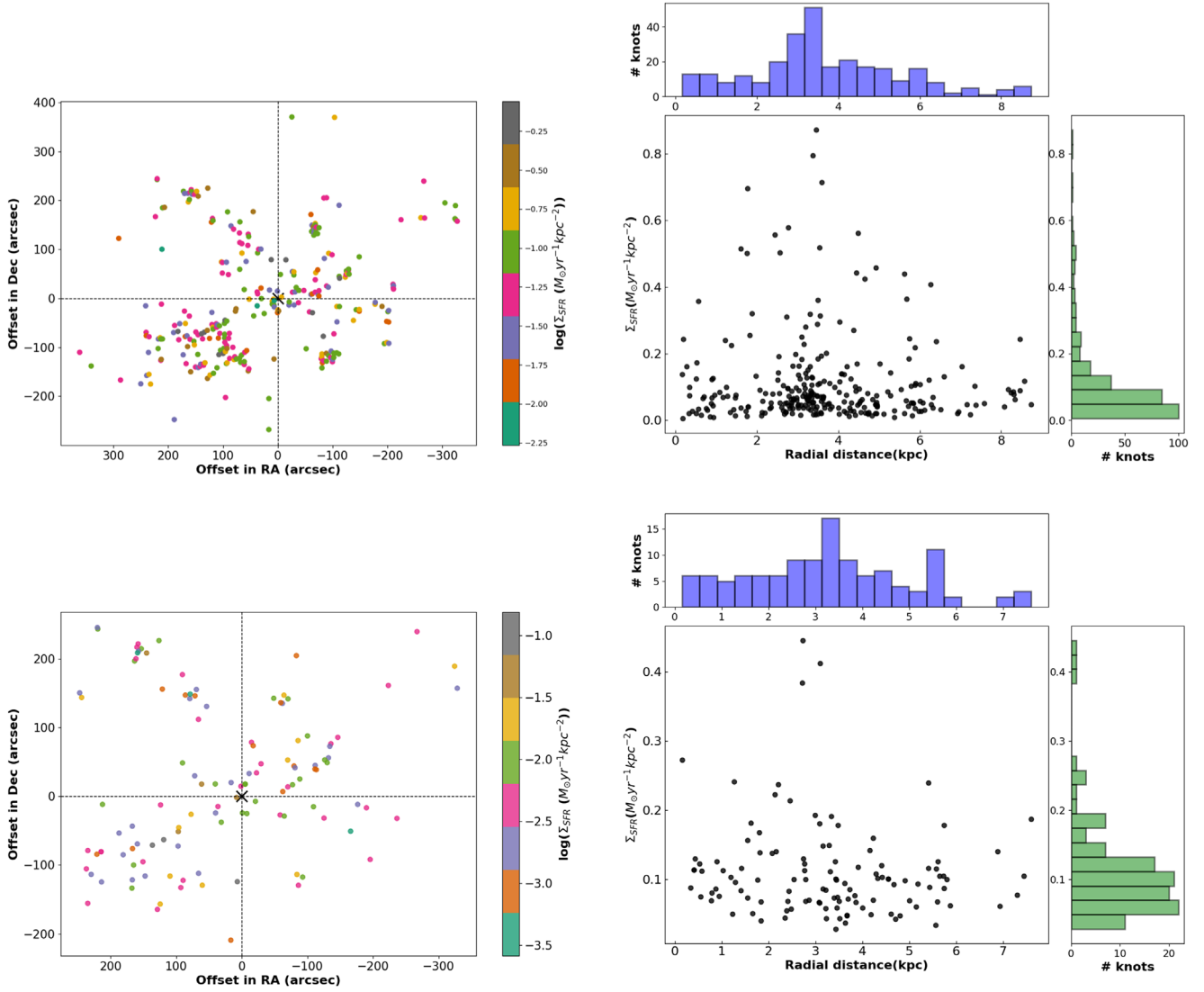
Figure 5. Distribution of $\Sigma_{\rm SFR}$ and its spatial variation in F148W (top panel) and Hα (bottom panel). Here, the central AGN is marked as a cross in the left panels.

following relation

$$\beta = \frac{m_{\rm FUV} - m_{\rm NUV}}{-2.5 \log(\lambda_{\rm FUV}/\lambda_{\rm NUV})} - 2.0. \tag{3}$$

Here $m_{\rm FUV}$ and $m_{\rm NUV}$ are the Milky Way extinction-corrected magnitudes in the F172M and F219M filters, respectively, and $\lambda_{\rm FUV}$, $\lambda_{\rm NUV}$ are the central wavelengths of the F172M and F263M filters, respectively, as tabulated in Table 2. Using the slope obtained in Equation (3), we calculated the color excess $E(B - V)$ in the SF regions as (Reddy et al. 2018)

$$\beta = -2.616 + 4.684 E(B - V). \tag{4}$$

From $E(B - V)$, we estimated the extinction A_λ as (Calzetti et al. 2000)

$$A_\lambda = k'(\lambda) E_s(B - V), \tag{5}$$

where $E_s(B - V) = (0.44 \pm 0.03)E(B - V)$ and $k'(\lambda)$ is defined as

$$k'(\lambda) = 2.659(-2.15 + 1.509/\lambda \\ - 0.198/\lambda^2 + 0.011/\lambda^3) + R'_V. \tag{6}$$

Here, $R_l V$ is 4.05 (Calzetti et al. 2000). For the filters F148W and N263M we obtained $k'(\lambda)$ of 10.411 and 7.568, respectively. The distribution of the internal extinction in the F148W and N263M filters as well as their spatial variation across NGC 4395 is shown in Figure 4.

To correct for internal extinction in Hα we adopted the following. We calculated β and $E(B - V)$ from the F172M and F219M filter images for these 120 regions, following Equations (3) and (4). We then evaluated A_λ for Hα with the k_λ' determined as follows (Calzetti et al. 2000)

$$k'(\lambda) = 2.659(-1.857 + 1.040/\lambda) + R'_V. \tag{7}$$

We obtained a value of $k'(\lambda)$ of 3.329. Using this we derived A_λ for all the 120 SF regions in Hα.

4. Properties of the SF Regions

4.1. SFR

The SFR provides important information on the assembly of stellar mass. As different populations of stars emit efficiently at different wavelengths, one needs to probe the SF regions in different bands. In particular, UV traces the emission from
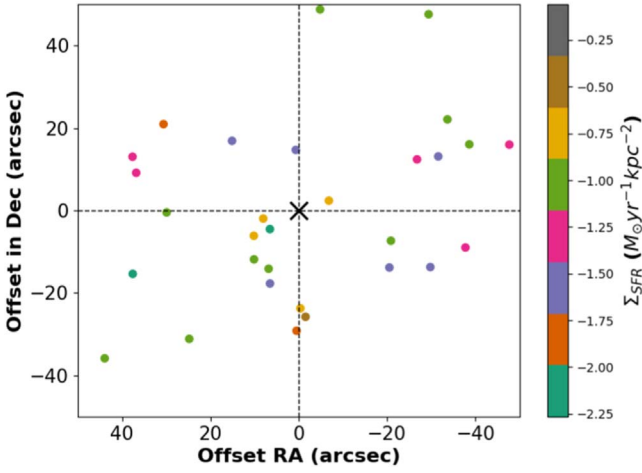
Figure 6. The variation of $\Sigma_{\rm SFR}$ in the central 100×100 square arcsecond region in the UV. The central AGN is marked as a cross in the figure.

young high-mass stars of O and B type (Davies et al. 2016), thereby providing best estimates of recent star formation over 100 Myr. Similarly, Hα traces star formation of <10 Myr (Kennicutt 1998; Kennicutt & Evans 2012; Calzetti 2013). Nearly half of the SF regions identified in the UV have also been detected in our observations in Hα. We estimated the SFR in the UV using the F148W filter using the following relation (Salim et al. 2007)

$$\log({\rm SFR}_{\rm FUV}(M_\odot\,{\rm yr}^{-1})) = \log[L_{\rm FUV}(W\,Hz^{-1})] - 21.16. \quad (8)$$

This relation (Equation (8)) traces a $0.1\,M_\odot$–$100\,M_\odot$ stellar population having a Chabrier initial mass function (IMF). We derived the SFR in Hα following the Kennicutt (1998) relation

$$\mathrm{SFR}(M_\odot\,\mathrm{yr}^{-1}) = 7.9 \times 10^{-42} L_{\rm H\alpha}(\mathrm{erg\,s}^{-1}). \quad (9)$$

Here, $L_{\rm FUV}$ is the intrinsic luminosity of the SF region in FUV and $L_{\rm H\alpha}$ is the luminosity of the SF region in Hα. The distribution of the SFR surface density ($\Sigma_{\rm SFR=SFR/Area}$) and its variation across the galaxy in F148W and Hα are given in Figure 5. The SFR calculated in the FUV filter spans a wide range from $2.0 \times 10^{-5}\,M_\odot\,{\rm yr}^{-1}$ to $1.5 \times 10^{-2}\,M_\odot\,{\rm yr}^{-1}$ with a median value of $3.0 \times 10^{-4}\,M_\odot\,{\rm yr}^{-1}$. In H$\alpha$ we found the SFR to range from $7.2 \times 10^{-6}\,M_\odot\,{\rm yr}^{-1}$ to $2.7 \times 10^{-2}\,M_\odot\,{\rm yr}^{-1}$ with a median value of $1.7 \times 10^{-4}\,M_\odot\,{\rm yr}^{-1}$. The $\Sigma_{\rm SFR}$ of the central 100×100 square arcsecond region in the F148W filter is shown in Figure 6.

4.2. Ages of the SF Regions

We calculated the ages of the SF regions using both the UV color (F148W − N263M) and Hα equivalent width.

4.2.1. UV Color

To determine the ages of the SF regions, we used the simple stellar evolutionary population model Starburst99 (Leitherer et al. 1999). We generated synthetic stellar spectra using Starburst99 by adopting a Kroupa IMF, a total stellar mass of $10^9 M_\odot$, solar metallicity, and ages up to 100 Myr. We convolved the generated UV spectra with the effective area of the respective UVIT filters to get the fluxes in the
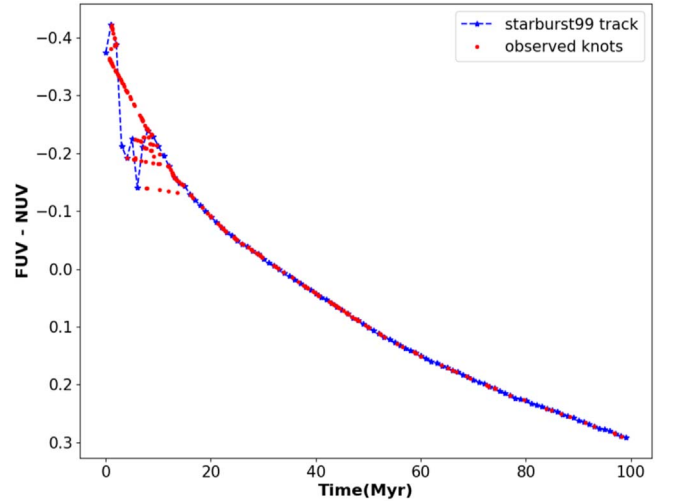
corresponding UVIT filters as

$$F^{\rm cal}(\lambda) = \frac{\int F(\lambda)\mathrm{EA}(\lambda)d\lambda}{\int \mathrm{EA}(\lambda)d\lambda}. \quad (10)$$

Here, EA(λ) is the effective area of each filter and $F^{\rm cal}(\lambda)$ is the simulated flux, which is then converted to an AB magnitude using the zero-points given in Tandon et al. (2020). The fluxes were then used to generate the theoretical colors. A plot of the age against the theoretical color is given in Figure 7. The observed FUV−NUV colors of the SF regions were compared with the theoretical colors to get the ages of the SF regions. The distribution of the ages of the SF regions obtained from the UV color, as well as its spatial variation in NGC 4395, are shown in the top panel of Figure 8.

4.2.2. Hα Equivalent Width

For the observations carried out in Hα, we determined the ages of the SF regions using the Hα equivalent width. Here too, we used the Starburst99 model (Leitherer et al. 1999) using the same input parameters as explained in Section 4.2.1. Starburst99 generates the expected equivalent width for different stellar populations at different timescales. We calculated the equivalent width from the calibrated narrowband Hα and nearest broad R-band continuum images using the following relation (Waller 1990)
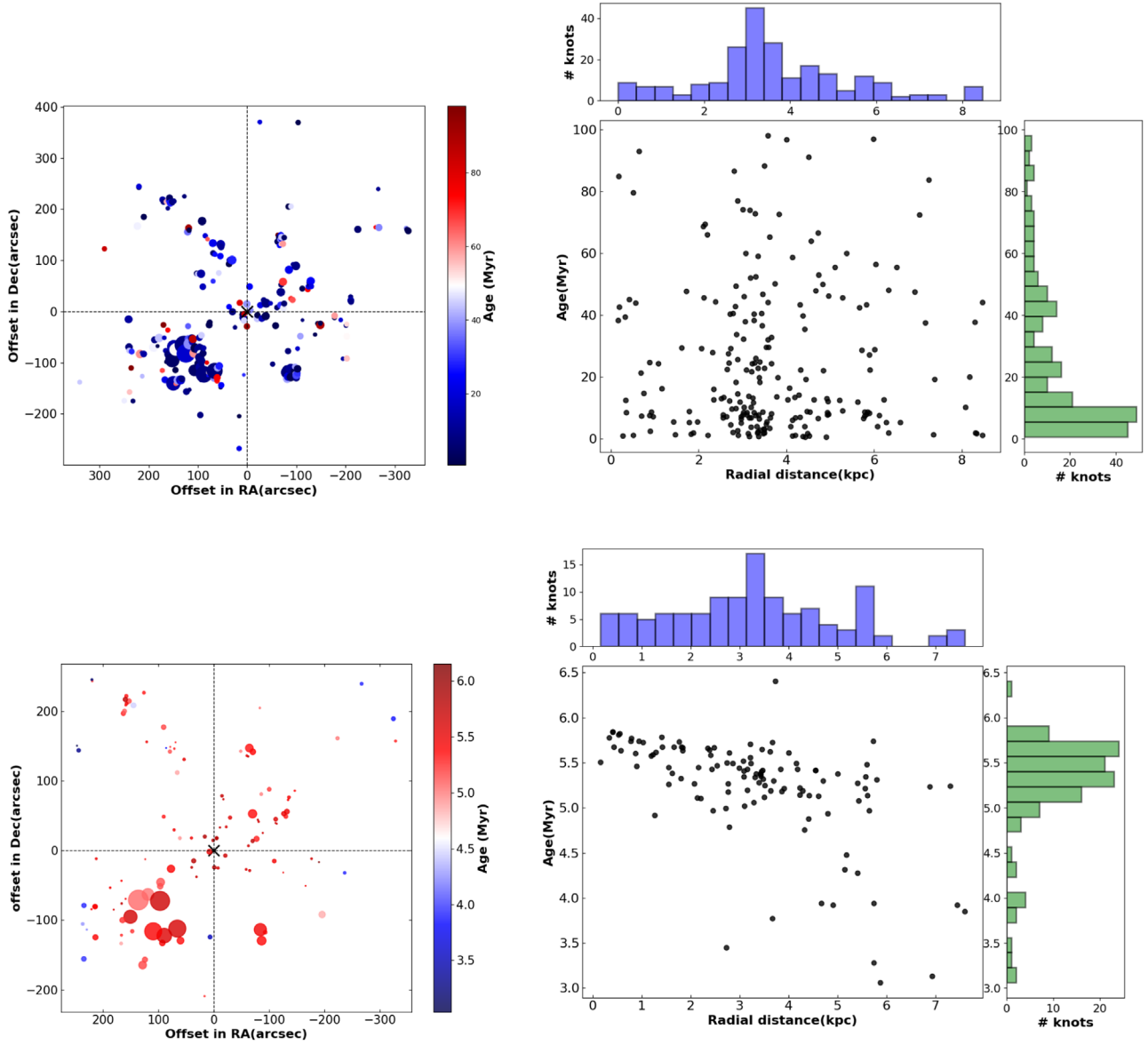
$$\mathrm{EW}_{\rm line} = \frac{[f_\lambda(N) - f_\lambda(B)]W(N)}{f_\lambda(B) - [f_\lambda(N)W(N)/W(B)]}. \quad (11)$$

Here, $f_\lambda(N)$ and $f_\lambda(B)$ are the flux densities measured in the narrowband Hα and broad R-band filters, respectively. Similarly, $W(N)$ and $W(B)$ are the bandwidths of the Hα line and broad R-band filters. The distribution of ages determined from the Hα observations is shown in the bottom panel of Figure 8.

4.3. Radial Dependences of the SFRs and Ages

The spatial distribution of the SF regions of varying ages can provide information on the impact that the local environment and

Figure 7. Extinction-corrected observed (FUV−NUV) color (red circles) against age. The blue dashed line is the synthetic track derived from a Starburst99 model.

Figure 8. Distribution of ages of the SF regions and their spatial variations in F148W (top panel) and Hα (bottom panel). In the left panel the different sizes of the points correspond to the sizes of the SF regions and the cross is the position of the central AGN.

the central AGN can have on the star formation characteristics of NGC 4395. To check for any such variation, we calculated the distance (R) and the deprojected distance (R') of the SF regions from the central AGN. The distance R' is calculated as

$$R' = \frac{R}{\sqrt{(\cos^2(\theta) + \sin^2(\theta)\cos^2(i))}}, \qquad (12)$$

where θ is given as

$$\theta = \cos^{-1}\frac{\delta\text{DEC}}{\sqrt{\delta\text{RA}^2 + \delta\text{DEC}^2}}, \qquad (13)$$

here, R is the observed distance from the center of NGC 4395, i is the inclination of the galaxy, and θ is the angle between the major axis of the galaxy and the radial distance to the SF region (Martin 1995; Gadotti et al. 2007). The variations of the ages of the SF regions obtained from the UV color, as a function of R', are shown in Figure 8. The distribution is random with no indication of variation of the ages of the SF regions with

distance as shown in the top panel of Figure 8. In the bottom panel of Figure 8 is the variation of the ages of the SF regions obtained from Hα as a function of galactocentric distance. There is a trend of young SF regions occupying regions at increasing distances from the central AGN. However, such a behavior is not seen in the UV. These different trends seen in the age versus radial distance in Hα and UV could be due to the different stellar populations probed by the integrated UV and Hα emissions. Any age gradients that might be in place during the short timescales (as probed by Hα), possibly are obliterated on the timescales probed by the UV (likely due to radial migration, etc.). The complete catalog of the SF regions identified in the UV is given in Table 3.

4.4. SFR at Multiple Wavelengths

The SFRs of the SF regions identified in NGC 4395 were estimated using observations carried out in the UV and Hα bands taking into account the differences in the instrumental

Table 3
Catalog of SF Regions in NGC 4395

No	R.A.(2000) (deg)	Decl.(2000) (deg)	a (arcsec)	b (arcsec)	PA (deg)	mag$_{FUV}$ (mag)	mag$_{NUV}$ (mag)	A$_{FUV}$ (mag)	A$_{NUV}$ (mag)	$\Sigma_{SFR}(M_\odot yr^{-1} kpc^{-2})$ FUV	NUV	Age$_{UV}$ (Myr)
1	186.548202	33.508548	1.61	1.08	−41.0	18.55	18.48	2.15	1.56	0.0895	0.0996	44
2	186.523056	33.498431	2.55	0.86	5.6	19.88	19.79	0.66	0.48	0.0209	0.0237	47
3	186.520573	33.542668	2.59	1.97	22.6	18.92	19.05	0.18	0.13	0.0215	0.0199	12
4	186.520348	33.527611	2.46	1.84	63.5	18.10	18.35	1.59	1.15	0.05183	0.04316	7
5	186.520043	33.503160	1.86	1.28	4.2	19.31	19.18	1.08	0.79	0.03217	0.03795	55
6	186.518845	33.525167	2.13	1.22	−61.3	18.92	18.94	1.05	0.76	0.04264	0.04354	28
7	186.518100	33.498277	1.57	1.05	−13.1	18.19	18.47	2.12	1.54	0.1316	0.1062	5
8	186.515629	33.593210	2.72	1.65	86.4	18.47	18.38	1.57	1.14	0.03743	0.04256	48
9	186.514743	33.614744	2.01	1.20	−32.0	18.92	19.02	0.76	0.55	0.04560	0.04367	19
10	186.514135	33.523861	3.35	1.17	−47.7	15.62	18.44	0.61	0.44	0.02881	0.03465	60

Note. Only the first ten entries are shown. Here, column 1 presents the index numbers of the detected regions. Columns 2, 3, 4, 5, and 6 are the R.A., decl., semimajor axis, semiminor axes, and position angles of the SF regions, respectively. Columns 7 and 8 are the extinction-corrected magnitudes in the F148W and N263M filters. Columns 9 and 10 present the extinction in the F148W and N263M filters. Columns 11 and 12 are the extinction-corrected surface density of the SFR in the F148W and N263M filters. And column 13 represents the age calculated in the UV. The table in full is available in the electronic version of the article.

(This table is available in its entirety in machine-readable form.)

resolutions in the UV and Hα. There are different calibration relations available in the literature (Kennicutt 1998; Salim et al. 2007; Brown et al. 2017) that pertain to observations at different wavelengths. It would be ideal for getting the SFRs of the SF regions identified in F148W and Hα at other wavelengths so that a comparison of the SFR estimates from different wavelengths could be made. But, for the regions identified in F148W and Hα it is not possible to get the SFR at other longer wavelengths, because of the poorer resolution at longer wavelengths.

An approach to compare the SFRs estimated at different wavelengths is to identify SF regions in images of different wavelengths at similar resolution. To achieve this, we used the image at 24 μm from Spitzer MIPS and smoothed the images of NGC 4395 acquired at other wavelengths such as the UV and optical bands to the spatial resolution of the 24 μm image. This was done using the task HGEOM in the AIPS software (Wells 1985). We then identified SF regions in the 24 μm image using the same procedure outlined in Section 3.1. We identified a total of 14 SF regions. We show in Figure 9 a composite image of NGC 4395 with the identified 14 regions marked by black ellipses on it. For these 14 SF regions, we calculated the SFR in the FUV, NUV, Hα, and 24 μm. For the UV and Hα we used the calibration relations given in Equations (8) and (9), respectively, while for 24 μm we used the following calibration relation (Brown et al. 2017)

$$\log(SFR_{24\mu m}) = [\log[L_{24\mu m}(erg\ s^{-1})] - 40.93]/1.3 - 1.26.$$
(14)

The results obtained from different wavelengths for these 14 SF regions are given in Table 4. The values of the SFR were estimated from the smoothed images, so that they have similar resolutions. Therefore, there will not be any effect of resolution on the estimated SFRs (given in Table 4) for different filters. Out of these 14 detected SF regions in IR, six SF regions (the 3rd, 6th, 7th, 8th, 9th, and 10th SF regions in Table 4) have higher SFRs at all wavelengths. In Figure 9 we have marked three SF complexes (A, B, and C) by white ellipses containing 3, 2, and 1 SF regions, respectively, detected based on the 24 μm band. These three SF complexes are known to be associated with SN remnants (Vukotic et al. 2005; Leonidaki
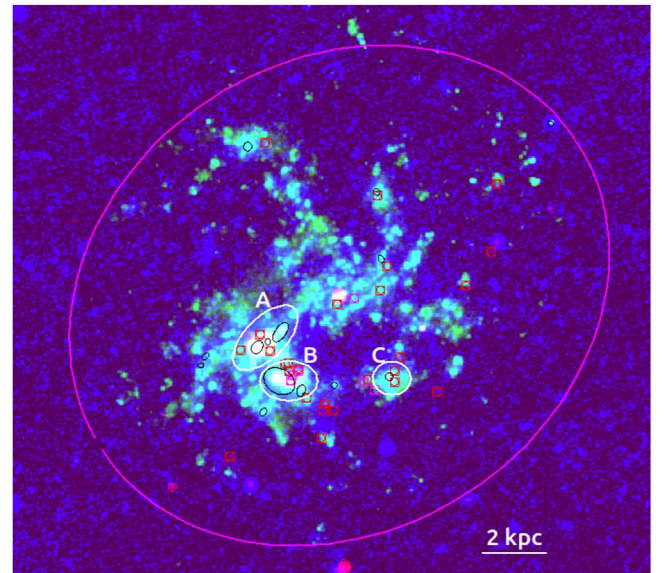
Figure 9. Composite image of NGC 4395 consisting of 1.4 GHz continuum (red), GALEX FUV (green), and 24 μm MIPS (blue). The identified SF regions based on the 24 μm image are overlaid on the image by black ellipses. The white ellipses marked by A, B, and C are the detected SF regions having counterparts at 1.4 GHz. The big magenta ellipse is the aperture equivalent to the D25 parameter in the optical U band. The red small boxes are the positions of SN remnants (Leonidaki et al. 2013).

et al. 2013). Using an aperture of 45 × 45 square arcseconds centered around the complexes A, B, and C we calculated the number density of resolved SF regions detected in the high-resolution UV image from UVIT-AstroSat and compared it with nearby 45 × 45 square arcsecond SN-free regions. In the regions centered around the complexes A, B, and C the average number density of the SF regions is 1.7×10^{-5} pc^{-2} whereas in the regions devoid of any known SNe, it is 0.7×10^{-5} pc^{-2}. The enhanced flux density and higher number of resolved SF regions in these three complexes (A, B, and C) could be thus attributed to positive feedback effects from SNe. As shown in Figure 10 the SF regions associated with A, B, and C have strong H I gas components, and also another SF region (13th in

Table 4
The SFR at Multiple Wavelengths Determined for the 14 SF Regions Identified in the MIPS 24 μm Image

No	R.A. (deg)	Decl. (deg)	a arcsec	b arcsec	PA (deg)	SFR (10^{-3} $M_\odot$ yr^{-1})			
						FUV	NUV	Hα	24 μm
1	186.488535	33.502065	6.06	4.24	57.5	0.152 ± 0.003	0.140 ± 0.002	0.717 ± 0.002	1.446 ± 0.333
2	186.455487	33.512476	4.37	4.09	−14.7	0.070 ± 0.002	0.063 ± 0.001	0.999 ± 0.002	1.677 ± 0.359
3	186.429978	33.515758	5.53	5.16	88.3	0.672 ± 0.014	0.646 ± 0.007	1.894 ± 0.003	1.182 ± 0.301
4	186.517630	33.520106	4.16	3.10	−2.6	0.023 ± 0.001	0.024 ± 0.001	0.070 ± 0.001	0.826 ± 0.252
5	186.515393	33.523667	5.97	3.67	42.76	0.071 ± 0.002	0.070 ± 0.001	0.179 ± 0.001	0.367 ± 0.168
6	186.491412	33.527326	9.88	7.319	52.35	2.9 ± 0.059	2.789 ± 0.031	13.493 ± 0.008	10.695 ± 0.906
7	186.486431	33.529412	4.51	3.76	−89.7	0.359 ± 0.008	0.362 ± 0.004	3.107 ± 0.004	2.532 ± 0.441
8	186.480444	33.533089	15.74	7.71	56.1	0.664 ± 0.014	0.689 ± 0.008	3.373 ± 0.004	3.757 ± 0.537
9	186.470888	33.510386	8.42	5.99	71.9	0.296 ± 0.006	0.303 ± 0.003	1.643 ± 0.003	1.728 ± 0.364
10	186.481081	33.514092	23.10	17.29	−30.1	4.178 ± 0.044	4.178 ± 0.044	12.080 ± 0.007	6.421 ± 0.702
11	186.433656	33.561573	5.94	4.02	−66.94	0.135 ± 0.003	0.128 ± 0.002	1.064 ± 0.002	0.934 ± 0.268
12	186.435697	33.587645	5.15	4.65	−37.0	0.297 ± 0.006	0.270 ± 0.003	1.021 ± 0.002	0.909 ± 0.264
13	186.495866	33.605167	6.37	5.72	64.5	0.206 ± 0.004	0.202 ± 0.002	0.862 ± 0.002	1.047 ± 0.283
14	186.354740	33.614038	3.97	3.53	6.4	0.125 ± 0.002	0.170 ± 0.002	0.006 ± 0.001	1.510 ± 0.340

Note. Here, a and b are, respectively, the semimajor and semiminor axes of the SF regions, while PA is the position angle.

(This table is available in machine-readable form.)

Table 4) marked as D has strong H I emission based on images from the WSRT (Heald & Oosterloo 2008).

4.5. Global SFR

In the earlier sections, we derived the SFRs as well as the ages for many SF regions identified in NGC 4395 utilizing scaling relations. Here, we aim to characterize the global SF nature of NGC 4395. For this, we decided to use two approaches using (a) the existing calibrations and (b) broadband spectral energy distribution (SED) modeling. Broadband SED modeling requires the brightness of the source to be evaluated at multiple wavelengths. For this we chose an aperture radius in the optical U band such that the surface brightness drops to 25 mag arcsec^{-2}. The same aperture was then used to estimate the brightness of NGC 4395 at different wavelengths, such as the GALEX FUV and NUV, optical U, B, V, R, and I from NOT, 2MASS J, H, and Ks, WISE W1, W2, and W3, and MIPS 24 μm, 70 μm, and 160 μm bands. A color composite of NGC 4395 in the UV, IR, and radio, with the aperture marked on it is given in Figure 9. The observed brightness of NGC 4395 at the 16 different wavelengths was used to generate a broadband SED which was then modeled using Code Investigating GALaxy Emission (CIGALE; Boquien et al. 2019) to derive different physical properties of NGC 4395.

We used CIGALE version 2022.0.[12] This code works on the principle of energy balance and uses a Bayesian analysis method to derive various model parameters. To build the model, we used the delayed star formation history with the optional constant burst/quench module, having the form SFR(t) $\propto$ $t \times$ exp($-t/\tau$) for $0 < t < t_0$. Here, t_0 is the age of the onset of star formation and τ is the time at which the SFR peaks. To model the stellar emission, we used the Bruzual & Charlot (2003) single stellar population template with Salpeter IMF. We used the Charlot & Fall (2000) model to take care of dust attenuation. The IR part of the SED, because of dust heated by stars, was taken into account by the use of the Draine et al. (2007, 2014) model and the presence of the AGN was
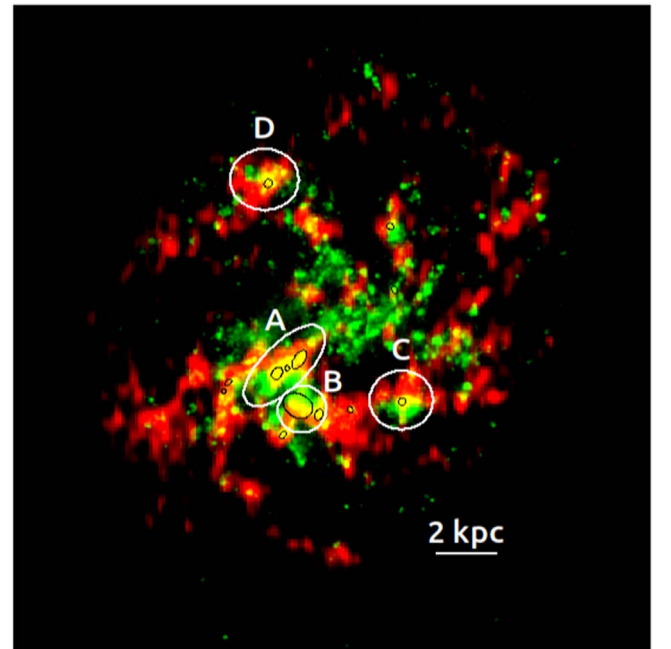
Figure 10. Composite image of NGC 4395 consisting of an H I line image (Heald & Oosterloo 2008; red) and GALEX FUV (green). Black ellipses are the identified regions from the 24 μm MIPS image. The white ellipses marked by A, B, C, and D are SF complexes with strong UV and H I emissions.

considered with the inclusion of SKIRTOR templates (Stalevski et al. 2016). The list of modules and the parameters used to build the SED of NGC 4395 are given in Table 5. The observed SED along with the model fit is given in Figure 11. Some of the derived parameters from fits to the SED are given in Table 6. We also derived the global SFR in the FUV, NUV, Hα, 24 μm, and 1.4 GHz using the scaling relations given in Equations (8), (9), (14), and (15) (Murphy et al. 2011)

$$\log(\text{SFR}_{1.4\text{GHz}}) = \log(L_{1.4}(\text{erg s}^{-1}.Hz^{-1})) - 28.20. \quad (15)$$

It is found that while the SFR obtained in the FUV, NUV, Hα, 1.4 GHz, and SED fitting are nearly in agreement with each

Table 5
Input Parameters for SED Fitting with CIGALE

Parameter	Value
Star formation history (sfhdelayedbq)	
e-folding time of the main stellar population	200.0, 500.0, 700.0, 1000.0, 2000.0, 3000.0, 4000.0, 5000.0 Myr
Age of the main stellar population	1500, 2000 Myr
Age of the late burst/quench episode	500 Myr
Ratio of the SFR after/before burst/quench	0.0, 0.1, 0.2, 0.4, 0.7, 1.0, 5.0, 10.0, 100.0
Instance without any burst	1.0
Stellar population synthesis (bc03)	
IMF	Salpeter
Metallicity	0.008, 0.02, 0.05
Separation between the young and the old stellar populations	10 Myr
Nebular emission (nebular)	
Ionization parameter	−2.0
Electron density	100 cm^{-3}
Dust attenuation (dustatt _ modified _ CF00)	
V-band attenuation in the interstellar medium (ISM)	0.05, 0.10, 0.15, 0.2, 0.5
AV_ISM / (Av_BC + Av_ISM)	0.50
Power-law slope of the attenuation in the ISM	−0.7
Power-law slope of the attenuation in the birth clouds	−0.7
Filters for which the attenuation will be computed and added	FUV and NUV
Dust emission (dl2014)	
Mass fraction of polycyclic aromatic hydrocarbon (PAH)	1.12, 2.5, 3.19, 5.26
Minimum radiation field	1.0, 10, 15, 25
Power-law slope	1.5, 2.0
Fraction illuminated from Umin to Umax	0.001, 0.01, 0.1, 0.5
AGN module (skirtor2016)	
Average edge-on optical depth at 9.7 μm	3, 7
Power-law exponent that sets the radial gradient with the polar angle	1.0
Index that sets the dust density gradient with the polar angle	1.0
Inclination, i.e., viewing angle, position of the instrument w.r.t. the AGN axis	30, 70
Disk spectrum	Skirtor spectrum
AGN fraction	0.0, 0.05, 0.1, 0.2, 0.3, 0.4
Wavelength range in microns used to compute the AGN fraction	0/0
Extinction law of the polar dust	SMC
$E(B-V)$ for the extinction in the polar direction in magnitudes	0.0, 0.03, 0.2, 0.4
Temperature of the polar dust	100.0 K
Emissivity index of the polar dust	1.6

other, as well as reported by Lee et al. (2009), the SFR obtained at 24 μm is lower. A summary of these results is given in Table 7. As can be seen in Table 7, SFRs of about 0.5 $M_\odot$ yr^{-1} found from a few tracers are in agreement with each other. However, from the 24 μm IR emission we obtained a SFR of 0.05 $M_\odot$ yr^{-1}, which is in agreement with the value of the SFR of 0.03 $M_\odot$ yr^{-1} found by Smirnova et al. (2020). This value is lower than that found from other tracers such as the FUV, NUV, Hα, and 1.4 GHz. The lower SFR at 24 μm is due to a lower intrinsic luminosity at 24 μm than that predicted by the flux (predicted 24 μm luminosity $\sim$10 times the observed 24 μm luminosity) from the Hα luminosity by Kennicutt et al. (2009) for SF galaxies. The SFR calculated from the predicted luminosity at 24 μm is similar to that obtained from other tracers.

5. Discussion

Recent theoretical studies point to AGN feedback operating in dwarf galaxies (Koudmani et al. 2022), which is also supported by observations (Penny et al. 2018). We have carried out a multiwavelength investigation on the star formation characteristics of the dwarf galaxy NGC 4395 to understand star formation and the effect of the AGN on the ISM of the host galaxy. Within 15″ from the center of NGC 4395, we noticed three SF regions having high SFRs in the UV. The high star formation in these regions in close proximity to the AGN could be because of positive feedback from the AGN. From SED model fits we obtained an AGN fraction around 0.1 (see Table 6), which also points to the contribution of the AGN to the observed properties. Alternatively, such enhanced star formation close to the AGN can happen if gas can be funnelled into the center of the galaxy by the presence of a bar and/or tidal interaction. However, in the case of NGC 4395, we do not have evidence of a bar or tidal interaction. Using the stellar mass as returned by our CIGALE modeling of the galaxy and SFR obtained from the FUV, we calculated the specific SFR (sSFR = SFR per unit mass). We found a value of sSFR = 4.64×10^{-10} yr^{-1}. This is larger than that of M33
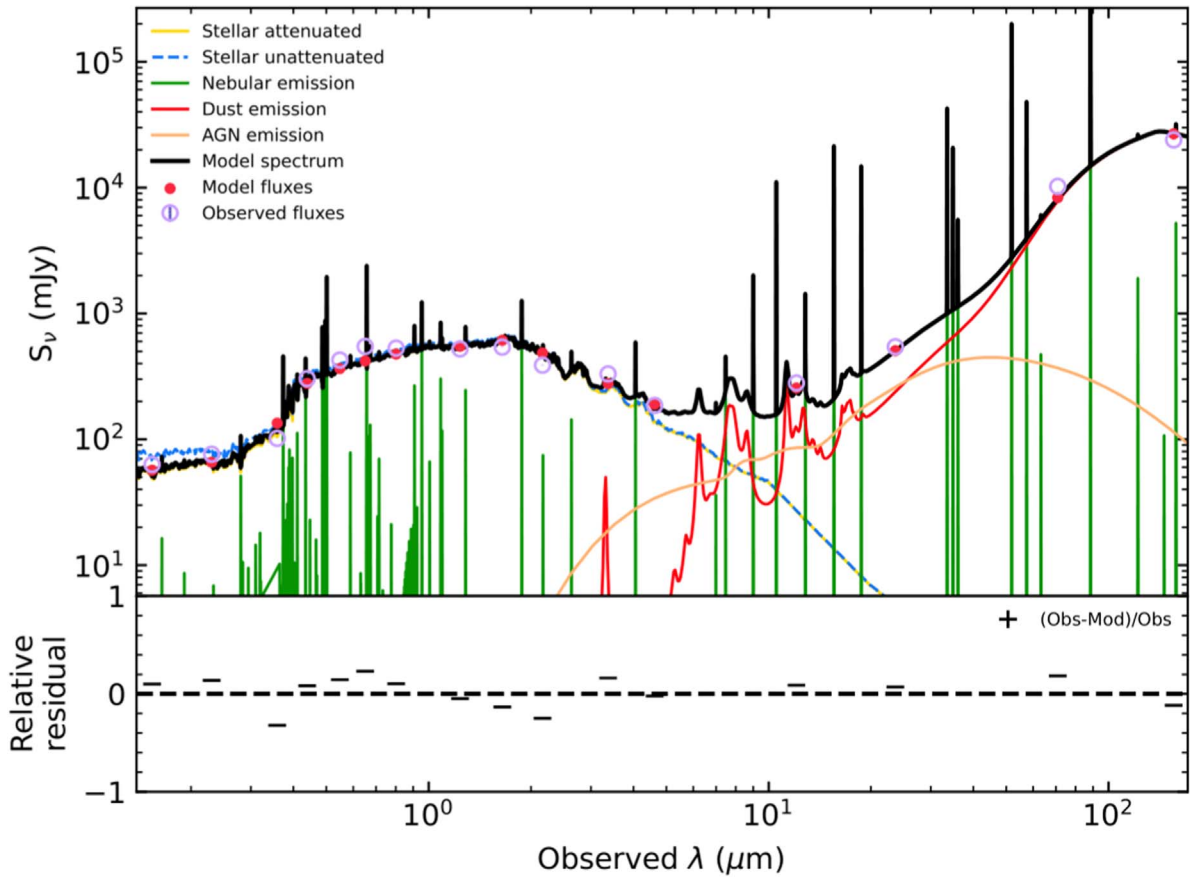
Figure 11. SED fitting using the CIGALE code for the whole galaxy.

Table 6
Parameters Derived from the Broadband SED Analysis

Parameter	Value
Stellar mass ($M_\odot$)	1.01×10^9
SFR ($M_\odot$ yr^{-1})	0.21 ± 0.02
SFR$_{100\ Myr}$ ($M_\odot$ yr^{-1})	0.21 ± 0.02
SFR$_{10\ Myr}$ ($M_\odot$ yr^{-1})	0.21 ± 0.02
Attenuation (Av_ISM)	0.1
AGN fraction	0.1

Table 7
Summary of the SFR Obtained at Different Wavelengths

Tracer	SFR ($M_\odot$ yr^{-1})
FUV	0.47 ± 0.00
NUV	0.55 ± 0.00
Hα	0.32 ± 0.00
24 μm	0.05
1.4 GHz	0.52
SED	0.21 ± 0.02

Note. A value of 0.0 in the error of the SFR means that the value is less than 1×10^{-3}.

(sSFR $= 1.13 \times 10^{-10}$ yr^{-1}; Corbelli 2003; Verley et al. 2009) and the LMC (sSFR $= 7.41 \times 10^{-11}$ yr^{-1}; van der Marel et al. 2002; Harris & Zaritsky 2009). These galaxies have stellar masses ($M_*|_{M33} = 4 \times 10^9$ $M_\odot$; Corbelli 2003; and $M_*|_{LMC} = 2.7 \times 10^9$ $M_\odot$; van der Marel et al. 2002)

similar to that of NGC 4395. We noticed a gradual decrease in the ages of the SF regions in Hα from the center toward the outer regions; however, this is not seen in the SF regions identified in the UV.

At 1.4 GHz we identified three SF complexes with enhanced radio emission marked as A, B, and C in Figure 9. These SF complexes encompass a few resolved SF regions seen in the IR and UV showing higher SFR. Also, the number densities of the resolved SF regions identified in the high-resolution UV are higher in these regions than the surroundings. Massive stars in these SF regions can affect the ISM through stellar winds and SN explosions. SN explosions could have an impact on the ISM, which could be either positive feedback by enhancing star formation (Hensler 2014) or negative feedback by inhibiting star formation (Gelli et al. 2023); however, the details are highly uncertain.

All the three SF complexes, A, B, and C, are known to be associated with SN remnants (Vukotic et al. 2005; Leonidaki et al. 2013). The high SFR and high number density of SF regions seen in SF complexes A, B, and C could be due to positive feedback effects from SNe. Alternatively, one would also expect higher SN rates in areas of high star formation due to stellar feedback processes. However, we found many regions that have an SN remnant without any associated bright SF region (see Figure 9). It is probable that the high SFRs seen in the SF complexes A, B and C are due to positive feedback from SNe. However, we note here that, just by the spatial coincidence of SNe and massive SF regions vis-a-vis isolated SNe not spatially coincident with SF regions, so it is difficult to conclude that SN explosions

could have caused the high SFRs via positive feedback. This is because stars are known to migrate from their birth places, which is also supported theoretically (Minchev et al. 2018). Therefore, one needs to account for the effects of radial migration before any conclusive claims on SN-induced positive feedback effects could be made. However, the SF regions in complex A (regions 6, 7, and 8 in Table 4), complex B (regions 9 and 10 in Table 4) and complex C (region 3 in Table 4) have higher SFRs in Hα and 24 μm (see Table 4) compared to the other SF regions, which could be due to compression of the ISM during SN explosions, arguing for SN-induced star formation, as in the case of NGC 2770 (Michałowski et al. 2020).

We found that cold neutral gas (H I) is extended throughout the spiral arms of the galaxy. However, there is no one-to-one correspondence between the SF regions traced by the UV and H I, although the peaks of H I emission (Heald & Oosterloo 2008) are associated with regions of high star formation and strong UV flux. To have a more detailed understanding of the relationship between the UV and H I emission, H I observations with spatial resolution comparable to the UV are needed. Systematic investigation of the star formation characteristics of a large sample of dwarf galaxies is needed to enhance our understanding of the complex feedback processes (SN and/or AGN) operating in dwarf galaxies.

6. Summary

In this work, we have carried out UV and Hα observations to study the spatially resolved SF regions of the host of the dwarf galaxy, NGC 4395. In addition to the new observations in the UV and Hα, we also used archival data at UV, IR, and radio wavelengths. We have also studied the global star formation properties of NGC 4395 using UV, optical, IR, and radio data. The results of this work are summarized below:

1. Using UV data acquired from UVIT on board AstroSat, we identified a total of 284 SF regions from the F148W image, extending up to a distance of 9 kpc.

2. Of the 284 SF regions identified in the UV, 120 SF regions were also identified in the Hα continuum-subtracted image. The detection of fewer SF regions in Hα is attributed to the lower spatial resolution as well as the shallowness of the Hα image relative to the UV one.

3. We found the SFRs in F148W to lie between 2.0×10^{-5} $M_\odot$ yr^{-1} and 1.5×10^{-2} $M_\odot$ yr^{-1} with a median value of 3.0×10^{-4} $M_\odot$ yr^{-1}. Using UV observations we found the ages of the SF regions to vary between 1 Myr and 98 Myr with a median value of 14 Myr.

4. In Hα we found a median SFR of 1.7×10^{-4} $M_\odot$ yr^{-1} with values between 7.2×10^{-6} $M_\odot$ yr^{-1} and 2.7×10^{-2} $M_\odot$ yr^{-1}. For the SF regions in Hα, we found a median age of 5 Myr with values ranging from 3 Myr to 6 Myr.

5. We did not find any noticeable gradual variation of the ages or Σ_{SFR} values of the SF regions from the center to the outer regions of the galaxy in the UV.

6. For the ages of the SF regions determined from the Hα equivalent width we found an indication of a gradual decrease in their ages from the center of the galaxy outwards. This might be attributed to the intense SF regions seen in Hα in the spiral arms of NGC 4395.

7. On inspection of the spatial distribution of Σ_{SFR} in the UV (see Figure 6) we found three SF regions near the AGN having a high Σ_{SFR}. One out of the three SF regions in the UV is also found to have a high Σ_{SFR} in Hα (lower left of Figure 5) and a younger age (lower left of Figure 8). This could possibly hint at positive feedback from the AGN. We, however, note that further observations are needed to confirm this.

8. We identified 14 common SF regions in the UV to IR bands. Out of these 14, seven SF knots have associated H I emission.

9. We found the global SFR to about 0.5 $M_\odot$ yr^{-1} in the UV. This is consistent with the SFR determined from other tracers such as Hα and the 1.4 GHz radio continuum. We also calculated a sSFR of 4.64×10^{-10} yr^{-1} in NGC 4395, which is larger than the sSFR of other dwarf galaxies such as M33 and the LMC that have stellar masses similar to NGC 4395.

10. At 1.4 GHz, we found few complexes having enhanced radio emission. These complexes contain a larger number of SF regions, with the majority of them having higher SFRs. These complexes are known to host SN remnants. The SF regions in these complexes have higher SFRs in Hα and 24 μm, compared to other SF regions, arguing for SN-induced star formation.

ORCID iDs

C. S. Stalin ⓘ https://orcid.org/0000-0002-4998-1861
D. J. Saikia ⓘ https://orcid.org/0000-0002-4464-8023

---

[13] https://ui.adsabs.harvard.edu/
[14] https://ned.ipac.caltech.edu

S. Muneer ⊙ https://orcid.org/0000-0002-4024-956X
Dominika Wylezalek ⊙ https://orcid.org/0000-0003-2212-6045
R. Sagar ⊙ https://orcid.org/0000-0003-4973-4745
Markus Kissler-Patig ⊙ https://orcid.org/0000-0002-5908-1488

References

Agrawal, P. C. 2006, AdSpR, 38, 2989
Álvarez-Álvarez, M., Díaz, A. i., Terlevich, E., & Terlevich, R. 2015, MNRAS, 451, 3173
Baldassare, V. F., Geha, M., & Greene, J. 2020, ApJ, 896, 10
Benson, A. J., Lacey, C. G., Baugh, C. M., Cole, S., & Frenk, C. S. 2002, MNRAS, 333, 156
Bertin, E., & Arnouts, S. 1996, A&AS, 117, 393
Boquien, M., Burgarella, D., Roehlly, Y., et al. 2019, A&A, 622, A103
Bradley, L., Sipőcz, B., Robitaille, T., et al. 2020, astropy/photutils: v1.0.0, Zenodo, doi:10.5281/zenodo.4044744
Brown, M. J. I., Moustakas, J., Kennicutt, R. C., et al. 2017, ApJ, 847, 136
Brum, C., Diniz, M. R., Riffel, R. A., et al. 2019, MNRAS, 486, 691
Bruzual, G., & Charlot, S. 2003, MNRAS, 344, 1000
Calzetti, D. 2013, in Secular Evolution of Galaxies, ed. J. Falcón-Barroso & J. H. Knapen (Cambridge: Cambridge Univ. Press), 419
Calzetti, D., Armus, L., Bohlin, R. C., et al. 2000, ApJ, 533, 682
Calzetti, D., Kinney, A. L., & Storchi-Bergmann, T. 1994, ApJ, 429, 582
Cardelli, J. A., Clayton, G. C., & Mathis, J. S. 1989, ApJ, 345, 245
Charlot, S., & Fall, S. M. 2000, ApJ, 539, 718
Colina, L., Vargas, M. L. G., Delgado, R. M. G., et al. 1997, ApJL, 488, L71
Condon, J. J. 1992, ARA&A, 30, 575
Corbelli, E. 2003, MNRAS, 342, 199
Davies, L. J. M., Driver, S. P., Robotham, A. S. G., et al. 2016, MNRAS, 461, 458
Davies, R. I., Sugai, H., & Ward, M. J. 1998, MNRAS, 300, 388
de Vaucouleurs, G., de Vaucouleurs, A., Corwin, H. G. J., et al. 1991, Third Reference Catalogue of Bright Galaxies (New York: Springer)
Diniz, M. R., Riffel, R. A., Storchi-Bergmann, T., & Riffel, R. 2019, MNRAS, 487, 3958
Draine, B. T., Aniano, G., Krause, O., et al. 2014, ApJ, 780, 172
Draine, B. T., Dale, D. A., Bendo, G., et al. 2007, ApJ, 663, 866
Fabian, A. C. 2012, ARA&A, 50, 455
Fanelli, M. N., Collins, N., Bohlin, R. C., et al. 1997, AJ, 114, 575
Ferrarese, L., & Merritt, D. 2000, ApJL, 539, L9
Filippenko, A. V., & Ho, L. C. 2003, ApJL, 588, L13
Filippenko, A. V., & Sargent, W. L. W. 1989, ApJL, 342, L11
Gaia Collaboration, Vallenari, A., Brown, A. G. A., et al. 2022, arXiv:2208.00211
Gadotti, D. A., Athanassoula, E., Carrasco, L., et al. 2007, MNRAS, 381, 943
Gebhardt, K., Bender, R., Bower, G., et al. 2000, ApJL, 539, L13
Gelli, V., Salvadori, S., Ferrara, A., Pallottini, A., & Carniani, S. 2023, arXiv:2303.13574
Ghosh, S. K., Tandon, S. N., Singh, S. K., et al. 2022, JApA, 43, 77
Greene, J. E., Strader, J., & Ho, L. C. 2020, ARA&A, 58, 257
Gu, Q. S., Huang, J. H., de Diego, J. A., et al. 2001, A&A, 374, 932
Gültekin, K., Richstone, D. O., Gebhardt, K., et al. 2009, ApJ, 698, 198
Harris, J., & Zaritsky, D. 2009, AJ, 138, 1243
Haynes, M. P., Hogg, D. E., Maddalena, R. J., Roberts, M. S., & van Zee, L. 1998, AJ, 115, 62

Heald, G., & Oosterloo, T. A. 2008, in ASP Conf. Ser. 396, Formation and Evolution of Galaxy Disks, ed. J. G. Funes & E. M. Corsini (San Francisco, CA: ASP), 267
Hennig, M. G., Riffel, R. A., Dors, O. L., et al. 2018, MNRAS, 477, 1086
Hensler, G. 2014, in IAU Symp. 296, Supernova Environmental Impacts, ed. A. Ray & R. A. McCray (Cambridge: Cambridge Univ. Press), 265
Kennicutt, R. C., & Evans, N. J. 2012, ARA&A, 50, 531
Kennicutt, R. C. J. 1998, ARA&A, 36, 189
Kennicutt, R. C. J., Hao, C.-N., Calzetti, D., et al. 2009, ApJ, 703, 1672
Kormendy, J., & Richstone, D. 1995, ARA&A, 33, 581
Koudmani, S., Sijacki, D., & Smith, M. C. 2022, MNRAS, 516, 2112
Lee, J. C., Gil de Paz, A., Tremonti, C., et al. 2009, ApJ, 706, 599
Leitherer, C., Schaerer, D., Goldader, J. D., et al. 1999, ApJS, 123, 3
Leonidaki, I., Boumis, P., & Zezas, A. 2013, MNRAS, 429, 189
Lira, P., Lawrence, A., O'Brien, P., et al. 1999, MNRAS, 305, 109
Magorrian, J., Tremaine, S., Richstone, D., et al. 1998, AJ, 115, 2285
Martin, P. 1995, AJ, 109, 2428
Michałowski, M. J., Thöne, C., de Ugarte Postigo, A., et al. 2020, A&A, 642, A84
Minchev, I., Anders, F., Recio-Blanco, A., et al. 2018, MNRAS, 481, 1645
Muñoz Marín, V. M., Storchi-Bergmann, T., González Delgado, R. M., et al. 2009, MNRAS, 399, 842
Murphy, E. J., Condon, J. J., Schinnerer, E., et al. 2011, ApJ, 737, 67
Oke, J. B. 1990, AJ, 99, 1621
Penny, S. J., Masters, K. L., Smethurst, R., et al. 2018, MNRAS, 476, 979
Peterson, B. M., Bentz, M. C., Desroches, L.-B., et al. 2005, ApJ, 632, 799
Prabhu, T. P. 2014, PINSA, 80, 887
Reddy, N. A., Oesch, P. A., Bouwens, R. J., et al. 2018, ApJ, 853, 56
Reines, A. E. 2022, NatAs, 6, 26
Rieke, G. H., Young, E. T., Engelbracht, C. W., et al. 2004, ApJS, 154, 25
Riffel, R., Dahmer-Hahn, L. G., Riffel, R. A., et al. 2022, MNRAS, 512, 3906
Saikia, P., Körding, E., Coppejans, D. L., et al. 2018, A&A, 616, A152
Salim, S., Rich, R. M., Charlot, S., et al. 2007, ApJS, 173, 267
Schutte, Z., & Reines, A. E. 2022, Natur, 601, 329
Skrutskie, M. F., Cutri, R. M., Stiening, R., et al. 2006, AJ, 131, 1163
Smirnova, K. I., Wiebe, D. S., Moiseev, A. V., & Jozsa, G. I. G. 2020, AstBu, 75, 234
Stalevski, M., Ricci, C., Ueda, Y., et al. 2016, MNRAS, 458, 2288
Tandon, S. N., Postma, J., Joseph, P., et al. 2020, AJ, 159, 158
Tandon, S. N., Subramaniam, A., Girish, V., et al. 2017, AJ, 154, 128
Thim, F., Hoessel, J. G., Saha, A., et al. 2004, AJ, 127, 2322
Tody, D. 1986, Proc. SPIE, 627, 733
Tsai, M., & Hwang, C.-Y. 2015, AJ, 150, 43
van der Marel, R. P., Alves, D. R., Hardy, E., & Suntzeff, N. B. 2002, AJ, 124, 2639
Venturi, G., Cresci, G., Marconi, A., et al. 2021, A&A, 648, A17
Verley, S., Corbelli, E., Giovanardi, C., & Hunt, L. K. 2009, A&A, 493, 453
Vukotic, B., Bojicic, I., Pannuti, T. G., & Urosevic, D. 2005, SerAJ, 170, 101
Waller, W. H. 1990, PASP, 102, 1217
Wells, D. C. 1985, in Proc. the 1st Workshop, Data Analysis in Astronomy, ed. L. di Gesu et al. (New York: Plenum Press), 195
Woo, J.-H., Cho, H., Gallo, E., et al. 2019, NatAs, 3, 755
Wright, E. L., Eisenhardt, P. R. M., Mainzer, A. K., et al. 2010, AJ, 140, 1868
Wrobel, J. M., Fassnacht, C. D., & Ho, L. C. 2001, ApJL, 553, L23
Yang, J., Yang, X., Wrobel, J. M., et al. 2022, MNRAS, 514, 6215